Hindawi
Shock and Vibration
Volume 2023, Article ID 6225283, 20 pages
https://doi.org/10.1155/2023/6225283

Research Article

Antipenetration Performance of Multilayer Protective Structure by the Coupled SPH-FEM Numerical Method

Wenlong Yang,[1] **Renchuan Ye**,[2] **Peng Ren**,[1] **and Ali Tian**[1]

[1]*School of Naval Architecture and Ocean Engineering, Jiangsu University of Science and Technology, Zhenjiang 212100, China*
[2]*Ocean College, Jiangsu University of Science and Technology, Zhenjiang 212100, China*

Correspondence should be addressed to Ali Tian; tianali@just.edu.cn

Received 4 September 2022; Revised 6 April 2023; Accepted 11 May 2023; Published 6 July 2023

Academic Editor: Vasudevan Rajamohan

Multilayer composite structures have significant advantages in antipenetration protection. Problems such as element distortion are more likely to occur when the FEM is used to simulate the heterogeneous composite structure against penetration with large deformation. A coupled smoothed particle hydrodynamic (SPH)-FEM is proposed to simulate the antipenetration performance of multilayer protective structures under the penetration of high-speed hemispherical-nosed projectiles. The large deformation and broken areas are calculated by the SPH method, which overcomes the problem of element distortion in FEM. In other areas, the FEM is used to improve the calculation efficiency. The results indicated that simulating multilayer plates using the coupled SPH-FEM can achieve the ballistic limit and deformation that agree with the experiment. Moreover, the deformation of single-layer, in-contact double-layer, spaced double-layer, and sandwich target plates with a core layer of water was studied and discussed. The influence of the faceplate and core layer on the penetration resistance performance was discussed in this paper by applying LSDYNA to establish the model of 3D SPH-FEM and calculate the dynamic process. In addition, the relationship between initial-residual velocity, deformation, and damage failure behavior was obtained.

1. Introduction

In recent years, multilayer protective constructions have been studied by many scholars, and these investigations have included the material, the structure, numerical simulation methods, and so on. These factors have a significant influence on the ballistic limit, which can reflect the performance of the antipenetration of the multilayer structure. Different materials and structures have been studied by scholars, and their properties can help us analyze possible ways of enhancing the ballistic performance of the composite structures. Most of these were acquired by comparing the results of the numerical simulation with those of the experiment [1, 2].

For high-speed impact and penetration, the main research methods are experiments and the finite element method. Wei et al. [3–5] investigated how the blunt-, ogvial-, and hemispherical-nosed projectiles penetrated the steel and determined the influence of the air gap between layers and the number, order, and thickness of layers on the ballistic performance through experiments. Zhao et al. [6] studied the ballistic performance of Sandwich plates with a steel face-layer and aluminum foam core with the FEM; they obtained the relationship between the ballistic limit and face-layer/core thickness and core density. Ali et al. [7] studied the crashworthiness of the Sandwich plate based on the FEM and an experimental method. Ahmadi et al. [8] investigated the high-velocity impact behavior of the Sandwich plate with syntactic foam cores and FML skins through experiments and the FEM. Abbasi and Alavi Nia [9] studied the high-velocity impact behavior of Sandwich plates with AL skins and foam cores through experiments and the FEM and analyzed the influence of the foam core layer on ballistic resistance. Ren et al. [10, 11] conducted a series of experiments, FEM simulation, and theory to study the free vibration dynamic/damage behavior and ballistic resistance of Sandwich plates with metallic skins and soft cores.

However, high-speed penetration has the characteristics of large deformation and fragmentation, and with the improvement of protection design, composite structures, especially heterogeneous composite structures, have gradually become the main structural form of ballistic protection. When the traditional FEM is used to simulate the penetration resistance performance, it is more prone to the problem of large grid distortion, resulting in reduced calculation accuracy and even interruptions. SPH adopts Lagrange particles to describe the deformation, and it is an ideal numerical method in impact mechanics without relying on elements [12–14]. It was first applied in the fluid computation field and gradually applied to low- and high-velocity impact and penetration. Kwon and Monaghan [15] investigated the sedimentation of dust in a turbulent fluid by using the SPH method, which had a good agreement with experimental results. Deng et al. [16] successfully determined the way to decay and drive turbulence within a two-dimensional rectangular tank with rigid no-slip boundaries using the SPH method. This demonstrated that fluid modeled by particles can have a strong contact with a solid boundary.

There are many methods to use SPH coupling, which can be used to handle the problem in many fields where many researchers have made a great progress. Khayyer et al. [17] presented the corresponding ISPH-HSPH FSI solver for 3D composite structures and their interactions with incompressible fluids, which can be capable of handling large material anisotropies and discontinuities at material interfaces without the use of any artificial stabilizers/smoothing schemes. Feng and Imin [18] presented the KDF-SPH method, which has higher accuracy and better convergence than the traditional SPH method. Zhao et al. [19] put forward the PB-SPH method to simulate the fracture of the rock with preexisting flaws, and the results show that this method can be well applied to rock mechanics engineering.

However, since the SPH needs to search for neighboring particles and calculate the physical quantities of each particle, it is time-consuming, so its computational efficiency is lower than that of FEM. Therefore, the coupled SPH-FEM technology came into being. This review aims to use the coupled SPH-FEM to investigate the multilayer plates of metal steel and the Sandwich plate. Studying the multilayered plate with the coupled SPH-FEM not only needs to address the problem of contact but also needs to determine whether plates using different materials are suited to the SPH method. Xue et al. [20] investigated the influence of the panel thickness on the underwater low-speed impacting resistance performance of the pyramid lattice structure based on the coupled SPH-FEM method, and the results were in good agreement with those of the experiment. Wu et al. [21] studied rock-breaking behavior under water jet impact with the SPH-FEM, where SPH was used to simulate the water jet and the FEM was adopted to simulate the rock-breaking response, and the results illustrated the rock impact on the rock of the water jet and breaking. Zhong et al. [22] analyzed the dynamic impact response characteristics and inertia effect based on the coupled SPH-FEM and found that the UHPC concrete slab had good impact resistance; the results of the numerical simulation agreed with those of the experiment. Zhou et al. [23] investigated composite laminates impacted by bird-strike using the SPH-FEM, and the damaging modes of laminates and the energy variations of the bird impact on the laminated plate were analyzed. Zhang et al. [24] investigated how the shaped-charge jets impact the double shell, which is steel and SPS, and found that the polyurethane layer protected the second shell based on SPH-FEM. Wang et al. [25] investigated the intersection of the aircraft and the fragment field under dynamic conditions based on the FEM-SPH method. Scazzosi et al. [26] used the coupled SPH-FEM to investigate the high-velocity impact of a metal ball against the ceramic-based plate. Yongjun et al. [27] investigated the antipenetration performance of ceramic/fiber composite targets which were impacted by high-speed alloy spherical projectiles based on the method of combining FEM-SPH and a range of results were obtained. Cheng et al. [28] studied how the tungsten heavy alloy projectile with different velocities impacted the B_4C ceramic target by using the FEM-SPH method. Islam and Shaw [29] used the SPH method to investigate the monolithic plate penetrated by three different projectiles which were hemispherical, conical, and ogival, and analyzed the influence of the six damage models.

The coupled SPH-FEM was used in many aspects, but more investigations are needed into the impact and penetration of multilayered plates and Sandwich plates [30, 31], especially when using different materials. This paper aimed to investigate the antipenetration performance of single- and multilayer Sandwich plates impacted by a hemispherical-nosed projectile with the coupled SPH-FEM.

In this study, a coupled SPH-FEM simulated the antipenetration performance of single-, double-layer, and Sandwich target plates subjected to high-speed hemispherical-nosed projectiles. This paper includes three main contents: (1) coupled SPH-FEM theory, contact algorithm, and constitutive models; (2) validation of the coupled SPH-FEM used on high-velocity penetration for single- and multilayer target plates; (3) and the ballistic behavior and deformation of single-layer, in-contact double-layer, spaced double-layer, and Sandwich target plates.

2. Coupled SPH-FEM Theoretical

2.1. SPH Theory. SPH is a kind of meshless method of particles, a partial differential equation of the complete Lagrange method, and its essence lies in a discrete domain to disperse matter that needs to be calculated into particles with Lagrange properties. There is an interaction among particles through the smooth function to realize their mechanical analysis and calculation, and the discrete domain is continuous equation (1). $\langle f(r)\rangle$ is the kernel of the function approximation equation [32, 33].

$$<f(r)> = \int_{\Omega} f\left(r^{'}\right) W\left(r - r^{'}, h\right) \mathrm{d}r^{'}, \tag{1}$$

$$W\left(r - r^{'}, h\right) = \frac{1}{h}\theta\left\{\frac{\left(r - r^{'}\right)}{h(x, y)}\right\}, \tag{2}$$

where r is the space position vector, which represents the position of the particle in the Ω domain, h denotes the smooth length, $\mathrm{d}r'$ indicates the volume element of partial derivatives, $W(r - r^{'}, h)$ is the smooth function, and the smooth function is infinite if the h infinitely approaches 0, and this condition meets the Dirac function that δ is approaching infinity. The size of r_c determines the size of the influence domain of the smooth function.

Figure 1 shows an approximate diagram of continuous variables [16], the influence of each factor in the influence domain of continuous smooth on the smooth function, and in this diagram $r_c = \kappa h$, where κ denotes the smooth factor, and both κ and h determine the size of the influence of the domain of the smooth function.

In the influence domain, equation (3) is the particle approximation, which is the summation of particle estimates for the spatial derivatives of field functions; the equation indicates the summation of adjacent particles j of all particles i in the influence domain.

$$<f(r)> = \sum_{j=1}^{N} \frac{m_j}{\rho_j} f\left(r_j\right) \cdot \nabla W\left(r - r_j, h\right), \tag{3}$$

where m_j and ρ_i are the mass and density of particle j, respectively, and the N represents the number of the particle j in the domain of the particle i. Especially, the smoothing kernel function W should meet the following conditions:

$$\int_{\Omega} W\left(r - r^{'}, h\right) = 1, \tag{4}$$

$$\lim_{h \longrightarrow 0} W\left(r - r^{'}, h\right) = \delta\left(r - r^{'}\right), \tag{5}$$

$$W\left(r - r^{'}, h\right) = 0, \left|r - r^{'}\right| > \kappa h. \tag{6}$$

Equation (4) is the normalization condition which means that the integral of a smooth function needs to be equal to 1. Equation (5) indicates that smoothing kernel function will have Dirac delta function properties when the smoothing length goes to 0, as the Dirac delta function is difficult to be satisfied. Equation (6) is the condition of compact support, where κ determines the scope of the smooth function.

In this paper, the most common smoothing kernel function $W(r_i - r_j, h)$ which used by the SPH community, the cubic B-spline was adopted in LSDYNA and is given as follows:

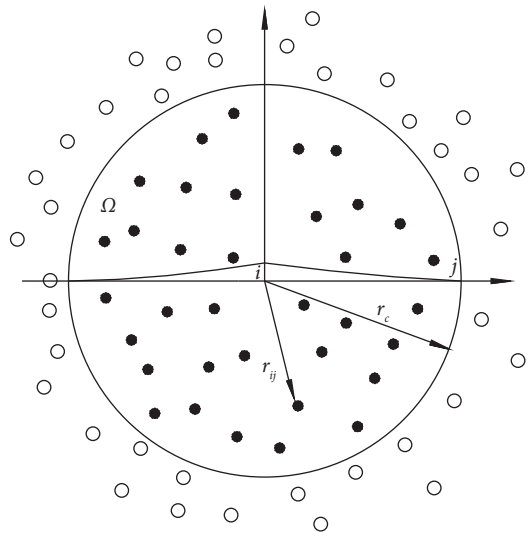

Figure 1: Approximation of the continuum variables (Ω: the support domain, and W is the smoothing kernel for particle i). In two-dimensional space, the support domain is a circle with a cutoff radius of r_c and r_{ij} is the distance between particle i and j [16].

$$W\left(r_i - r_j, h\right) = \alpha_D \times \begin{cases} \frac{2}{3} - D^2 + \frac{1}{2}D^3, & 0 \le D < 1, \\ \frac{1}{6}(2 - D)^3, & 1 \le D < 2, \\ 0, & D \ge 2, \end{cases} \tag{7}$$

in which α_D is $1/h$, $15/(7\pi h^2)$, and $3/(2\pi h^3)$ in one-, two-, and three-dimensional space, respectively. D is the relative distance between two points r_i and r_j [34]. The SPH formalism implies a derivative operator; a particle approximation for the derivative operator must be defined. Before giving the definition of this approximation, we define the gradient of a function as:

$$\nabla f(r) = \nabla f(r) - f(r)\nabla 1(r), \tag{8}$$

where 1 denotes the unit function.

The SPH formulation for hydrodynamics with material strength is expressed as follows:

$$\frac{dv^{\omega}}{dt} = \frac{1}{\rho}\frac{\partial \sigma^{\omega\zeta}}{\partial r^{\zeta}}, \tag{9}$$

where ω and ζ are space indices, v^{ω} is the velocity component, ρ is the density, $\sigma^{\omega\zeta}$ is the total stress tensor which consists of pressure and viscous stress, r^{ζ} is the spatial coordinates, and e is the internal energy. The above-mentioned conservation equations can be solved using weak discrete form, which of the conservation equations can be expressed as follows.

The particle approximation of the weak form of the momentum conservation equation is as follows:

$$\frac{\mathrm{d}v_i^{\alpha}}{\mathrm{d}t} = \sum_{j=1}^{N} m_j \left(\frac{\sigma_i^{\omega\zeta}}{\rho_i^2} + \frac{\sigma_j^{\omega\zeta}}{\rho_j^2} \right) \frac{\partial W_{ij}}{\partial r_i^{\zeta}}. \tag{10}$$

2.2. SPH-FEM Coupling Algorithm. The coupled SPH-FEM is realized using contact algorithms, and there are two coupling parts between FE and SPH: the attachment and the contact couple [34]. In this paper, the contact of particles and finite elements used tied contact, which adopted the kinematic constraint algorithm, and the penalty algorithm was used for the contact coupling. The abovementioned interface algorithms are both based on the master-slave scheme [35, 36]. In this scheme, the interface includes two sides, which are the slave and master sides, in three dimensions. As shown in Figure 2, the illustration of the interaction of slave point and master segment, which are the particles and finite elements, respectively, shows n_s is the master surface, and the slave point contacts the nearest master segment in the surface.

2.3. SPH-FEM Attachment Algorithm. The kinematic constraint algorithm plays an important role in the contact between the SPH and FE; Figure 3 shows the process of the kinematic constraint algorithm in the constraint interface [34]. The algorithm eliminates the normal degree of freedom of nodes by converting between nodes and imposing global constraints, which can reduce the explicit integration time and improve efficiency. When the particles were impacted in calculation, the interface of the contact of the slave nodes and master segment (finite elements) transformed the force to the master surface which were the finite elements, and caused the interaction of particles and finite elements. In addition, it will detect and update independently after each time step, and the interpolated contact point (ξ_c, η_c) on the master segment will keep the state at each time step. The following equations show the procedures for the increments of force and mass for the master nodes.

$$\Delta M_m^i = \phi_i(\xi_c, \eta_c) M_s, \tag{11}$$

$$\Delta f_m^i = \phi_i(\xi_c, \eta_c) f_s, \tag{12}$$

where $\phi_i(\xi, \eta)$ is the interpolation function, and i is the number of the master node.

After the summation of all slave nodes is completed, the acceleration of the k_{th} node of the master segment a_i^k can be obtained from the following equation:

$$a_{is} = \sum_{k=1}^{4} \phi_k(\xi_c, \eta_c) a_i^k, \tag{13}$$

where a_i^k is the master segment interface and k is the sequence of the nodes.

2.4. SPH-FEM Contact Algorithm. The contact between the SPH plate and the FE projectile is realized by the penalty method. In the process of the computation, the contact occurs only when the penetration becomes positive, so every single slave node ns will be checked for penetration l through the master surface [35].

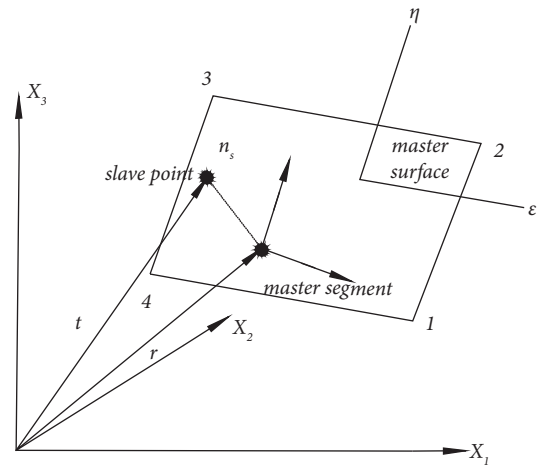

Figure 2: Location of contact point when n_s lies above the master segment [35].

$$l = n \times [s - m(\xi_c, \eta_c)] < 0, \tag{14}$$

where n is a vector normal to the master segment at the contact point (ξ_c, η_c). g and r are position vectors drawn to the slave node and master node, respectively.

If penetration l occurs ($l < 0$), an interface force vector f_s which is proportional to the magnitude of the penetration is applied between the slave node and its corresponding contact point.

$$f_s = -lk_i n_i. \tag{15}$$

Then, the interface force applied to the four nodes ($i = 1$, 2, 3, 4) of the master segment can be expressed as follows:

$$f_m^i = \phi_i(\xi_c, \eta_c) f_s, \tag{16}$$

$$k_i = \frac{f_{\mathrm{si}} K_i A_i^2}{V_i}. \tag{17}$$

Equation (16) $\phi_i(\xi_c, \eta_c)$ is the interpolation function. k_i is the stiffness factor for the master segment, f_{si} is the factor, K_i is the bulk modulus, A_i is the face area of the element, and V_i is the volume [35].

3. Validation of the SPH-FEM Method

In this section, a series of SPH-FEM numerical simulation validations were carried out on multilayer target plate material, and the projectiles were Q235 and 38CrSi steel. The numerical simulation process adopted the modified Johnson_Cook and Plastic_Kinematic constitutive models; the former was used to simulate the plate, and the latter was used to simulate the projectile. At the same time, water was added between the two layers of target plates to investigate its hindrance effect on projectile impact, which simulated the impact on a liquid tank of the projectile. Therefore, we

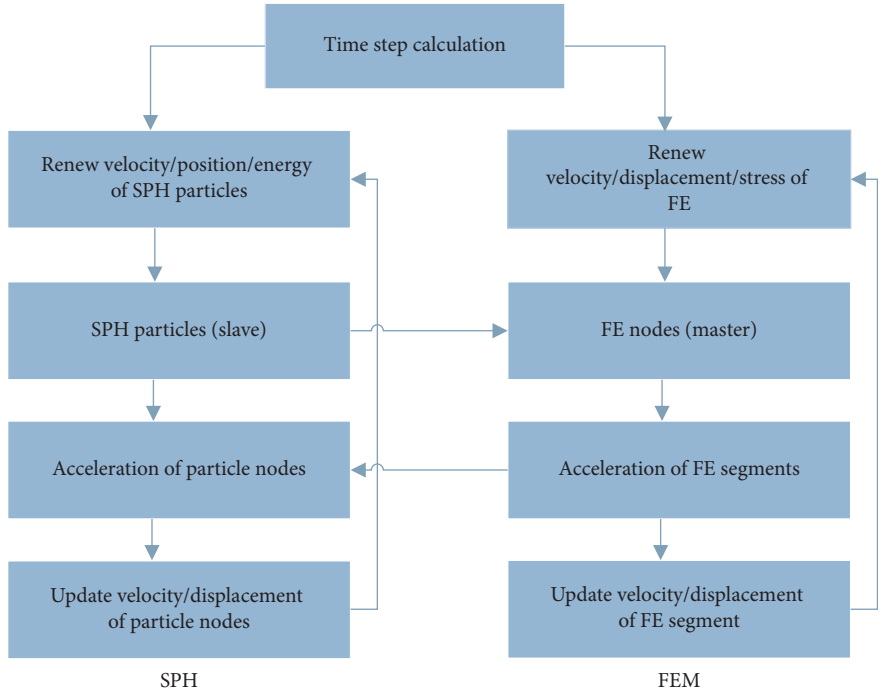

Figure 3: Calculation procedure for the SPH-FEM contact algorithm [34].

needed to verify the feasibility and accuracy of the coupled SPH-FEM by comparing it with the experimental results.

3.1. Material Parameters of the Target Plate and Projectile. The material of the multilayer target plates was Q235 steel. The constitutive model of the Q235 steel adopted MAT_-MODIFIED_JOHNSON_COOK, and this constitutive model is a well-known version in LSDYNA (material model 107) [37–39]. It is expressed as follows [38]:

$$\sigma_{\mathrm{eq}} = \left(A + B\varepsilon_{\mathrm{eq}}^{n}\right)\left(1 + \varepsilon_{\mathrm{eq}}^{*}\right)^{c}\left(1 - T^{*m}\right), \tag{18}$$

where σ_{eq} and $\varepsilon_{\mathrm{eq}}$ represent the equivalent stress and equivalent plastic strain, respectively. A, B, n, C, and m are the material constants; $\varepsilon_{\mathrm{eq}}^{*}$ indicates the dimensionless strain rate; and the homologous temperature is expressed as $T^{*} = (T - T_r)/(T_m - T_r)$, where T, T_r, T_m denote absolute temperature, room temperature, and melting temperature, respectively. The temperature increment from adiabatic heating is calculated as follows:

$$\Delta T = \int_{0}^{\varepsilon_{\mathrm{eq}}} \frac{\chi\sigma_{\mathrm{eq}}}{\left(\rho C_p\right)d\varepsilon_{\mathrm{eq}}}, \tag{19}$$

where ρ and C_p denote the density and specific heat, and χ denotes the Taylor-Quinney coefficient, which gives the proportion of work converted into heat [40]. The modified Johnson_Cook material model simulates the steel target impacted by the projectile [41], and the parameters of the material model are shown in Table 1 [42]. The constitutive model of the projectile is Plastic_Kinematic, as shown in Table 2 [43]. The constitutive model of water adopted the MAT_NULL in LSDYNA (material model 09) in Table 3 [44], and this constitutive model has no yield strength and is generally used in fluid material calculation.

3.2. Types and Geometry Parameters of Target Plate. The coupled SPH-FEM was used to simulate the hemispherical-nosed projectile penetrating a multilayer target plate in this paper; the particle was adopted in the center region of the target plate penetrated by the projectile, which is called the SPH domain, while the FEM was adopted in the remaining plates. The hemispherical-nosed projectile also adopted the FEM. Figure 4 shows the model states of the different target plates; the larger area in the middle is particle distribution, which is called the SPH domain, and the impervious part surrounding it remains in the form of a finite element mesh, which is called the FEM domain. The aim of this arrangement was to reduce the amount of calculation while ensuring its accuracy. The target plate configuration and codes are listed, in Table 4; the symbol "T" represents the thickness of the plate, and "T2" indicates that the thickness of the plate is 1 mm.

The numerical simulation model of the T4 target plate and projectile is shown in Figure 4(a), where the single-layer target plate thickness was 2 mm. According to the character of SPH, the smaller the space between the particles, the larger the interaction among them [45], so the space between two particles of the plate was 0.9 mm. As is shown in Table 5 the relative error was the smallest, and the rest of the plate, which was the FEM domain, had a mesh size of 3 mm. A total of 16,200 particles were used to simulate the vulnerable part, and the sum of the number of remaining mesh nodes of the target plate and the elements of the projectile was 45,936. The numerical simulation models of the first and the second

Table 1: Material constitutive and damage parameters for Q235 steel [42].

ρ (kg/m^3)	E (GPa)	ν	T_r (K)	T_m (K)	A (MPa)	B (MPa)	n
7800	200	0.3	300	1795	229	439	0.503
C	m	$\dot{\varepsilon}(s^{-1})$	χ	cp	D_1	D_2	D_3
0.1	0.55	1.1×10^{-3}	0.9	469	0.3	0.9	−2.8

Table 2: Material constitutive and damage parameters for projectile [43].

ρ (kg/m^3)	E (GPa)	ν	σ_0	E_t
7850	204	0.33	1900	15000

Table 3: Material constitutive and damage parameters for water [44].

ρ (kg/m^3)	pc (Pa)	MU (N·S·m^{-2})
998.21	−10.0	$0.8684E-3$

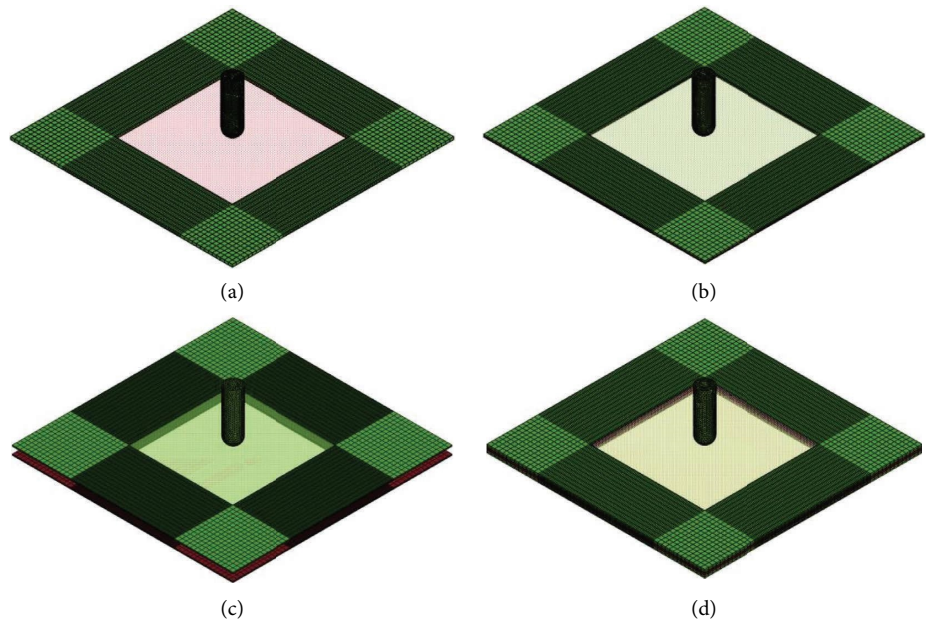

Figure 4: SPH-FEM model of different types of target plates and hemispherical-nosed projectile. (a) Target plate (T4) and projectile model. (b) Target plate (T2T2) and projectile model. (c) Target plate (T2_6_T2) and projectile model. (d) Target plate (T4T4T4) and projectile model.

Table 4: The target plates configuration and codes.

Target plate numbers	Target plate codes	Thickness (mm)	Explanation
1	T4	2	Single-layer plate
2	T2T2	1 + 1	In contact double-layer plate
3	T2_6_T2	1 + 6 (air) + 1	Spaced double-layer plate
4	T4T4T4	2 + 2 + 2	In contact three-layer plate

layer T2T2 (1 mm + 1 mm) target plates are shown in Figure 4(b). The model included two steel target plates with the same thickness of 1 mm, in which the total number of particles was 16,200, and the sum of the number of remaining mesh nodes of the target plate and the elements of the projectile body was 45936.

The numerical simulational model of the T2_6_T2 (1 mm + 6 mm +1 mm) target plate and projectile is shown in Figure 4(c); two 1 mm steel plates separated by 6 mm air space, in which the number of particles was 4418 and the sum of the number of remaining mesh nodes of the target plate and projectile was 57727. The numerical simulational

Table 5: The convergence of target plates.

The particle spaces (mm)	The relative error (%)	Calculating time	Explanation
0.7	134.85	35 h 21 min	Single-layer plate
0.8	54.735	30 h 10 min	Single-layer plate
0.9	4.22	20 h 12 min	Single-layer plate
1	11.26	18 h 13 min	Single-layer plate
1.1	15.96	16 h 10 min	Single-layer plate
1.5	95.425	4 h 20 min	Single-layer plate

model of the *T4T4T4* (2 mm + 2 mm +2 mm) target plate and projectile is shown in Figure 4(d), which is represented as three identical steel target plates contacted together; each plate thickness was 2 mm, the number of particles was 48,600, and the remaining mesh nodes of the target plate and projectile element numbers were 129,136. The distance between the projectile and the target plate was 0.1 mm to reduce the movement distance of the projectile before contact. The projectile was hemispherical-nosed with a diameter of 12.62 mm and a total length of 39.91 mm.

3.3. Boundary Conditions. The boundary condition for the coupled SPH-FEM was *CONTACT_TIED_NODES_SURFACE_ CONST-RAINED_OFFSET*, which can be used to transfer the force received by the particle to the finite element nodes. The contact method adopted by the projectile when penetrating the target plate was *CONTACT_AUTOMATIC_NODES_TO_SURFACE*, which ensures a good contact effect between particles and the projectile surface. The projectile made an active contact with the plate and made contact with every finite element per node, and the nodes applied forces to the finite element mesh in the contact process.

3.4. Velocity Validation of the SPH-FEM Method. In this study, the coupled SPH-FEM was used to investigate the antipenetration performance of the target plate. The feasibility and accuracy of the coupled SPH-FEM were validated by comparing them with experimental results [5]. The relationship between initial and residual velocities was obtained based on the least squares fitting method, and the analytical model of ballistic limit velocity first proposed by Recht and Ipson [46] is expressed as follows:

$$v_r = a\left(v_i^p - v_{\mathrm{bl}}^p\right)^{1/p}, \tag{20}$$

where v_i is the initial impact velocity of the projectile, v_r and v_{bl} are the residual velocity of the projectile and ballistic limit velocity respectively. In this paper, the formula was used to get the fitting data for the residual velocity. Tables 6 and 7 show the comparison of the ballistic limit velocities of the experiment and the numerical simulation for different plates, and the results of the ballistic limit of the experiment and the simulation respectively were very close. $a = m_p/(m_p + m_{pl})$ and m_p and m_{pl} are the masses of projectiles and plugs, respectively. Both a and p are fitted to the numerical simulation result using the method of least squares [4].

Table 6: Experiment of model constants and ballistic limit velocity.

Target plate codes	a	p	v_{bl} (m/s)
T4	0.9	2.6	133.8
T2T2	0.96	2.56	127.8
T2(6)T2	0.98	2.45	112.8
T4T4T4	0.92	2.63	285

Table 7: Numerical simulation of model constants and ballistic limit velocity.

Target plate codes	a	p	v_{bl} (m/s)
T4	0.736	3.122	133.73
T2T2	0.6982	3.31	127.46
T2(6)T2	0.95	2.145	111.51
T4T4T4	0.75	3.42	270.6

Comparisons of the SPH-FEM numerical and experimental results for T4, T2T2, T2_6_T2, and T4T4T4 target plates are shown in Figures 5(a)–5(d). It can be concluded that the initial-residual velocity of the coupled SPH-FEM method showed good agreement with the experimental initial-residual velocity.

3.5. Deformation Validation of SPH-FEM

3.5.1. Comparison of the Deformation Curve and Process of Different Target Plates. In order to validate the single-layer target plate deformation accuracy of the coupled SPH-FEM, the deformation results of the SPH-FEM and the experiments were analyzed and compared. The comparison of the deformation profiles of the experiment and the SPH-FEM simulation for the T4 target plate is shown in Figure 6, and the deformation history is shown in Figure 7. It can be seen in Figure 6 that the simulational deformational profiles of SPH-FEM had a good agreement with the experimental results, but there were differences in the maximum deformation and small deformation regions. These occurred because the experimental models were rigidly fixed by bolts, and the SPH-FEM numerical simulations were fixed in the four boundary surfaces. In addition, the SPH particle numbers were finite, and the particle numbers and particle distance had some effect on fragmentation and maximum deformation. It can be seen in Figure 7 that the target plate deformation process was nearly the same between the SPH-FEM simulation and experiment; the only difference was the location of the plug, because the projectile could not

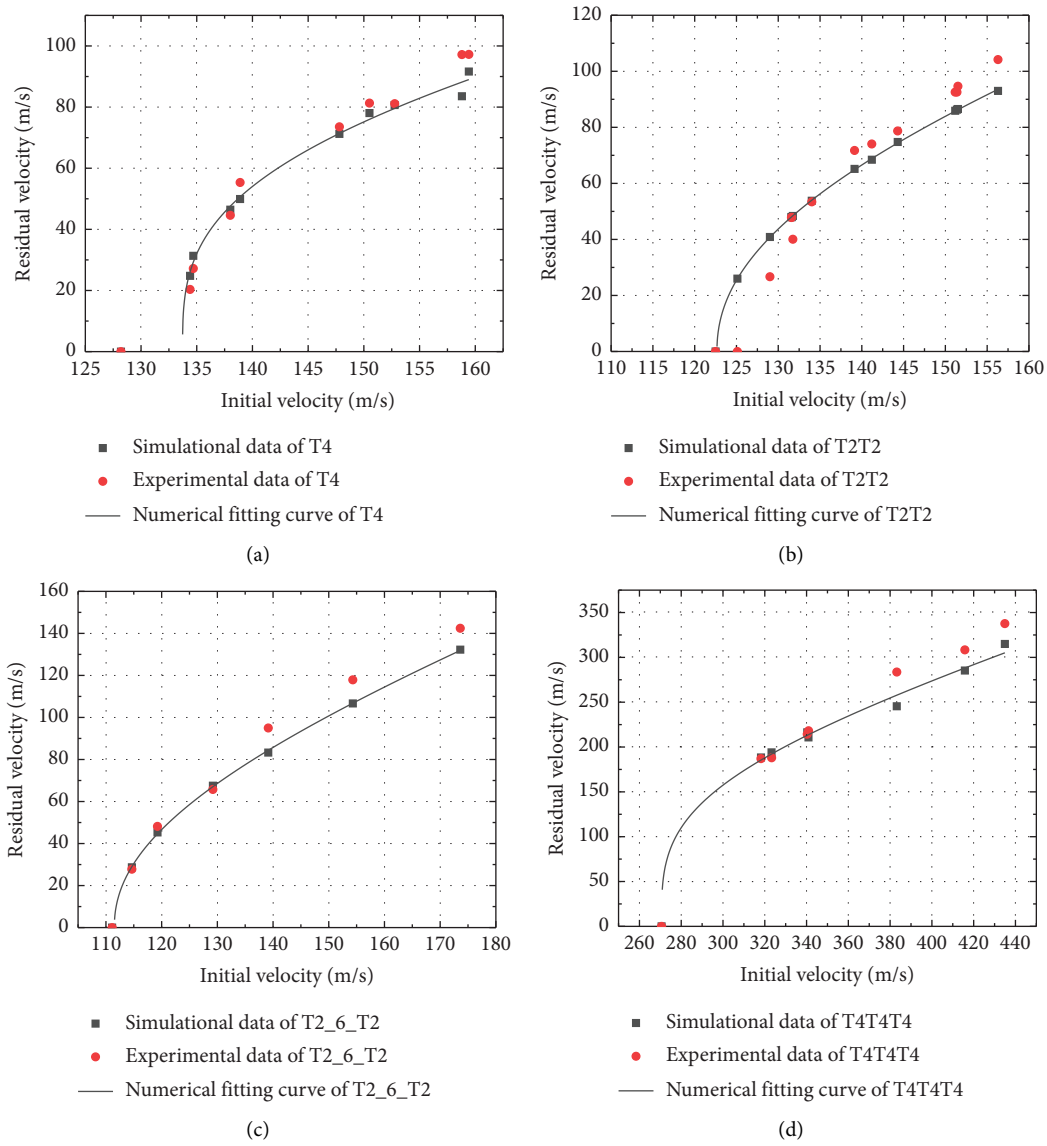

Figure 5: Residual velocity versus initial velocity of different target plates. (a) T4. (b) T2T2. (c) T2_6_T2. (d) T4T4T4.

remain completely horizontal during flight in the experiment, so the experimental plug did not move away from the target plate.

In order to validate the contact algorithm and deformation process accuracy of the in-contact double-layer target plate, the T2T2 and T2_6_T2 target plates were simulated by the coupled SPH-FEM, and comparisons of the deformation profiles of the numerical simulation and the experiment are shown in Figure 8 and Figure9, and the deformation history is shown in Figure 10. We see in Figure 8 that the simulational deformational profiles of SPH-FEM had a very good agreement with the experimental deformations; there were differences in the small deformational region, which was the coupling place of particles and the finite mesh. It can be seen in Figure 10 that the target plate deformation process was almost the same between the SPH-FEM simulations and the experiment; the only difference was the size of the plug, owing to the influence of the particle numbers and particle distance. Thus, we can prove that the coupling SPH-FEM accurately simulated the contact and deformational processes of the multilayer contact target plate.

3.5.2. Comparison of Deformation of Numerical Simulation and Experiment. The relationship between the hemispherical-nosed projectile's initial-residual velocity, deformation, and damage to target plates was determined. Therefore, we need to compare the deformation results of different target plates in the numerical simulation and the experiment. [5] Figure 11 shows the deformation states of the in-contact double-layer target plate T2T2. Figures 11(a) and 11(b) are the first and second target plates in the numerical simulation of T2T2, and Figures 11(c) and 11(d) are the first and second target plates in the experiment; neither of them produced the plug, and the deformations were almost the same.

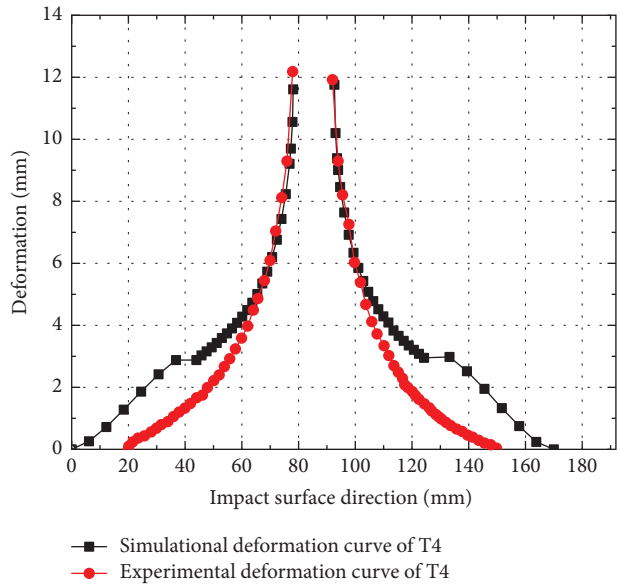

Figure 6: Comparison of deformation profiles of experiment and simulation for T4 target plate (simulation: T4 $v_i = 138.89$ m/s, $v_r = 49.93$ m/s; experiment: T4 $v_i = 138.89$ m/s, $v_r = 55.35$ m/s [5]).

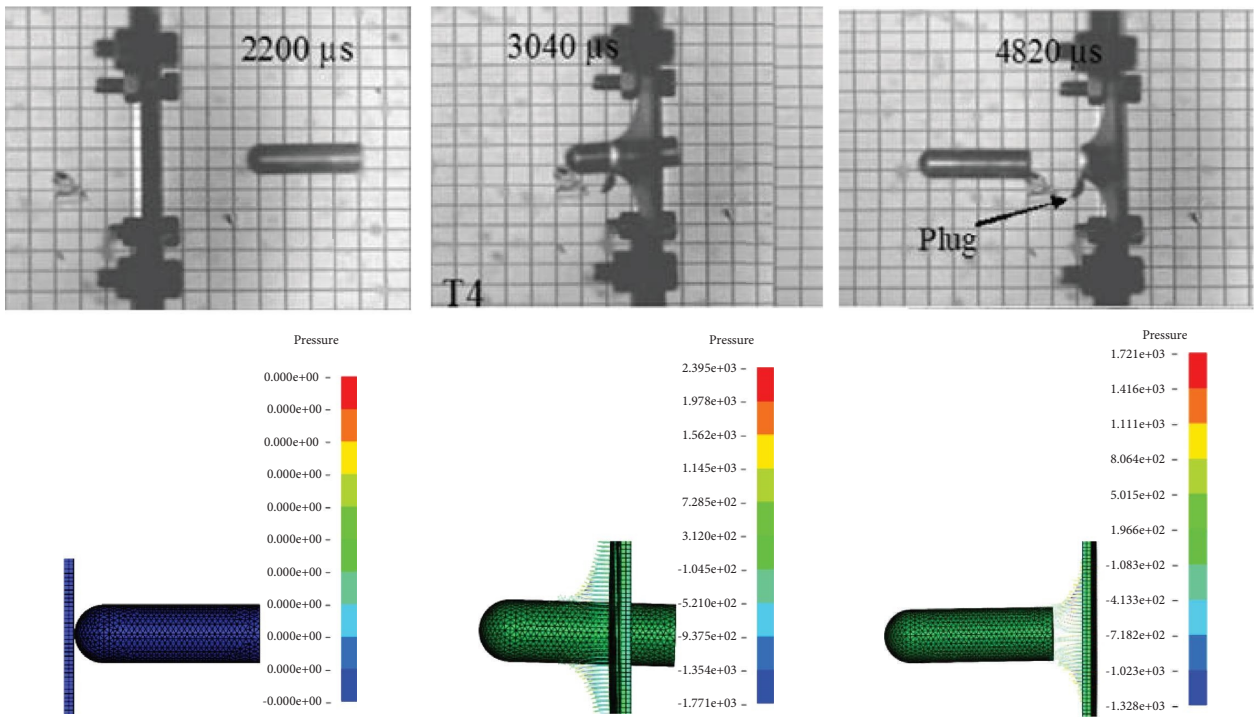

Figure 7: Comparison of deformation history of experiment and simulation for T4 target plate (simulation: T4 $v_i = 134.46$ m/s, $v_r = 20.33$ m/s; experiment: T4 $v_i = 134.4$ m/s, $v_r = 24.79$ m/s [5]).

Figures 12(a)–12(c) show the separate deformation states of the first, second, and third plates of the in-contact three-layer target plate T4T4T4 in the numerical simulation, and Figures 12(d)–12(f) show the separate deformation states of the first, second, and third plates of the in-contact three-layer target plate T4T4T4 in the experiment. From the diagrams, we know that they experienced dishing and bending deformation and all produced the plug, which had nearly been broken down upon impact with the relatively higher-speed projectile. The plugs produced by the numerical simulation were broken because the velocity of the projectile was so high that the force applied to the nodes was great, and after comparing them, the results of the numerical simulation were a good agreement with experimental results.

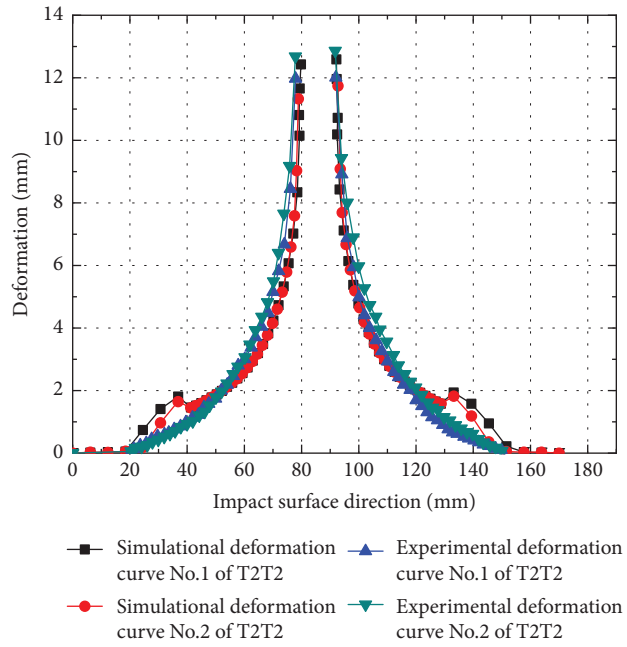

Figure 8: Comparison of deformation profiles of experiment and simulation for T2T2 target plate (simulation: T2T2 $v_i = 139.13$ m/s, $v_r = 65.17$ m/s; experiment: T4 $v_i = 139.13$ m/s, $v_r = 71.76$ m/s [5]).

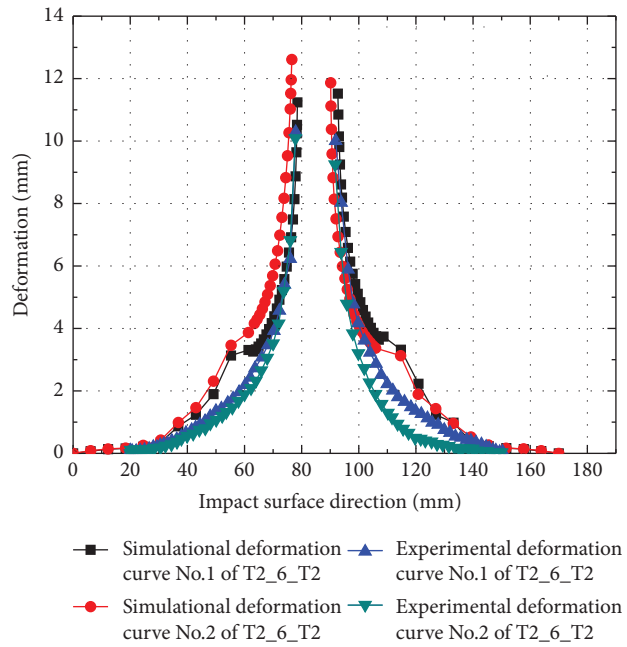

Figure 9: Comparison of deformation profiles of experiment and simulation for T2_6_T2 target plate (simulation: T2_6_T2 $v_i = 139.14$ m/s, $v_r = 83.28$ m/s; experiment: T2_6_T2 $v_i = 139.14$ m/s, $v_r = 94.97$ m/s [5]).

4. Antipenetration Analysis of Single- and Double-Layer Sandwich Target Plate

In this section, the results for the single target plate T8, the in-contact double-layer target plate T4T4, the spaced double-layer target T4_12_T4 and the spaced double-layer target T4_water_T4 are investigated based on the validated coupled SPH-FEM. First, the penetration processes of the four types of target plates are presented and analyzed, and the influences of target plate thickness, air gap, and water gap on the dynamic process are obtained. Second, the initial-residual velocity relationships of the four different types of target plate are studied, and the influences of target plate thickness, air gap and water gap on residual velocity are obtained. Finally, the deformation is investigated, and the influences of target plate thickness, air gap, and water gap on deformation and damage are obtained.

4.1. Models of Single- and Double-Layer and Sandwich Target Plate. The coupled SPH-FEM was validated in Section 3. On this basis, the antipenetration performances of the single-layer, in-contact double-layer, spaced double-layer, and Sandwich target plates are investigated. The numerical models of the target plate T8 (4 mm), target plate T4T4 (2 mm + 2 mm), and target plate T4_12_T4 (2 mm + 12 mm +2 mm) are shown in Figures 13(a)–13(d), respectively. The models separately represent the single target plate T8, meaning the thickness is 4 mm, and the aim was to maintain the thickness consistency of the different target plates: the in-contact target plates with a thickness of 2 mm and the spaced double-layered target plate with the same 2 mm thickness separated by 12 mm air fluid. The sum of the number of particles was 32,400, and the number of finite elements in the target plate and hemispherical-nosed projectile was 87,536.

The numerical model of the T4_water_T4 (2 mm + 12 mm +2 mm) target plate and projectile is shown in Figure 13(e). The thickness of the front and back steel target plates of this model was 2 mm, and the thickness of the water in the middle was 12 mm. And between them, the number of particles was 189,399, and the remaining mesh part of the target plate and the projectile body element was 324,336. It should be pointed out that the number of particles in the water was 156,999, and the number of grid nodes of the water tank was 216,000.

The overall size of the target plate was 170 mm × 170 mm, and the thickness of the target plate differed according to the different target plate types. T4 denoted that the thickness of the target plate was 2 mm, and the thickness of the later target plate was the same, while the size of the middle particle part was 90 mm ∗ 90 mm. The particle spacing of 0.9 mm corresponded to the grid cell size, while the mesh element size of the residual target plate was 3 mm, and the mesh size of the projectile was set to 1.3 mm. The distance between the projectile and the target plate was 0.1 mm to reduce the movement distance of the projectile before contact. The hemispherical-nosed projectile had a diameter of 12.62 mm and a total length of 39.91 mm.

4.2. Process Analysis of Projectile Penetration Target Plate. The penetration process of the hemispherical-nosed projectile on the single-layer target plate T8, the in-contact double-layer target plate T4T4, the spaced double-layer target plate T4_12_T4 with 12 mm air fluid and

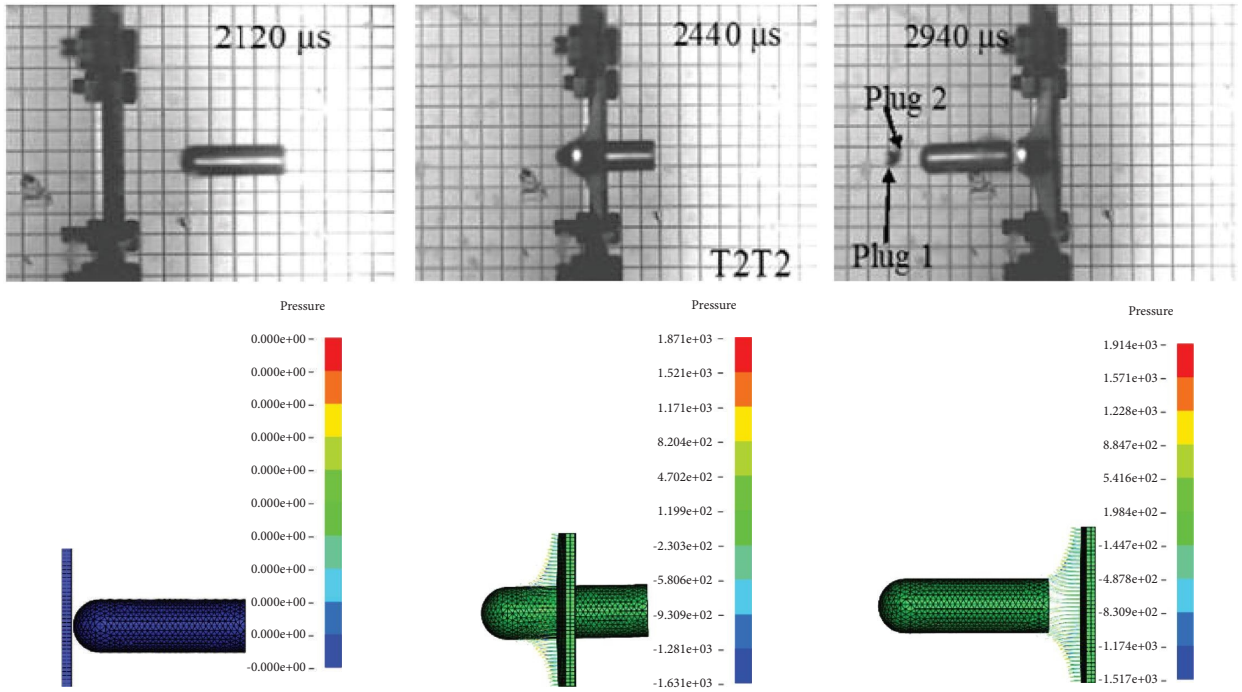

FIGURE 10: Comparison of deformation history of experiment and simulation for T2T2 target plate (simulation: T2T2 $v_i = 141.2$ m/s, $v_r = 74.07$ m/s; experiment: T4 $v_i = 141.2$ m/s, $v_r = 68.45$ m/s [5]).

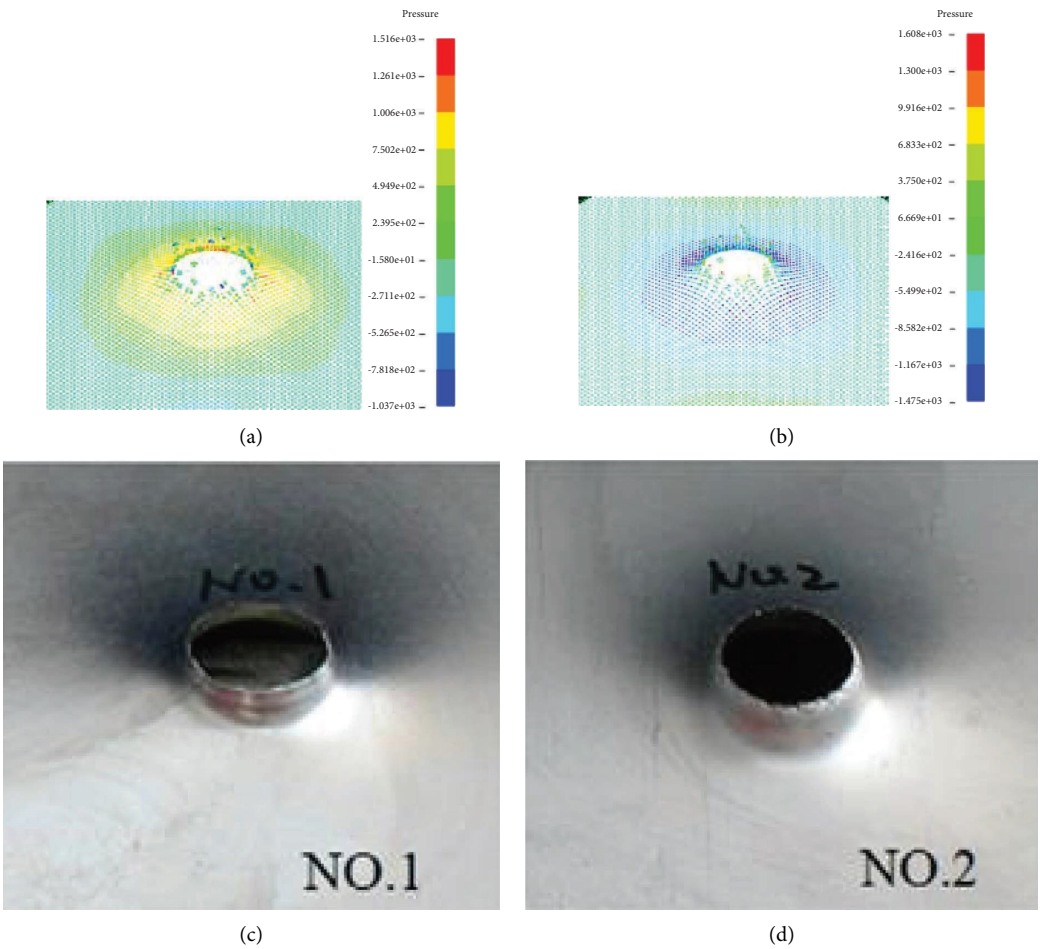

FIGURE 11: The comparison of target plate T2T2 for numerical simulation and experiment [5] (*a*, $bv_i = 139.13$ m/s, $v_r = 65.17$ m/s; *c*, $dv_i = 139.13$ m/s $v_r = 71.76$ m/s). (a) NO. 1. (b) NO. 2. (c) NO. 1. (d) NO. 2.

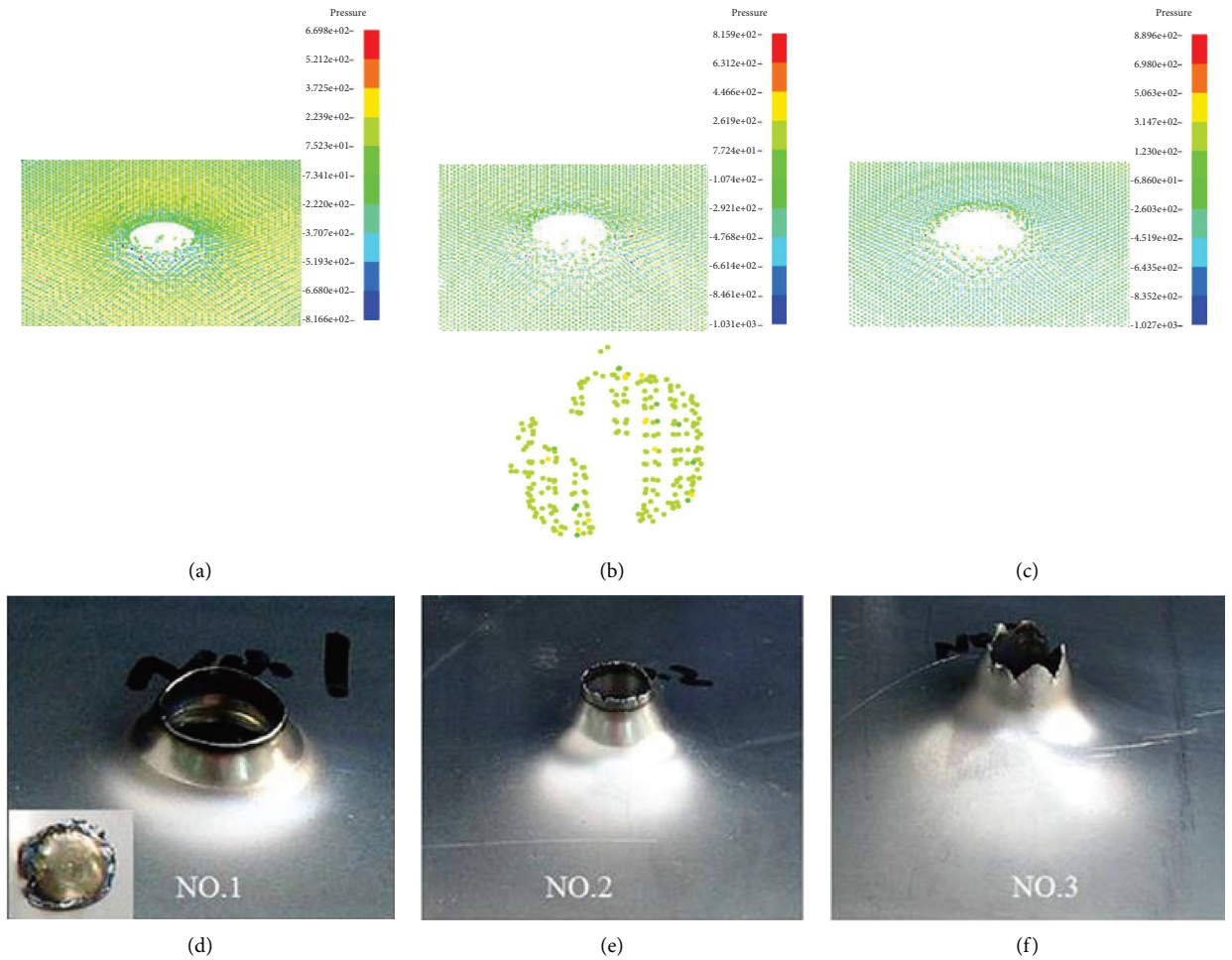

FIGURE 12: The comparison of target plate T4T4T4 for numerical simulation and experiment [5] (*a*, *b*, $cv_i = 340.91$ m/s, $v_r = 210.73$ m/s; *d*, *e*, $fv_i = 340.91$ m/s $v_r = 214.29$ m/s). (a) NO. 1. (b) NO. 2. (c) NO. 3. (d) NO. 1. (e) NO. 2. (f) NO. 3.

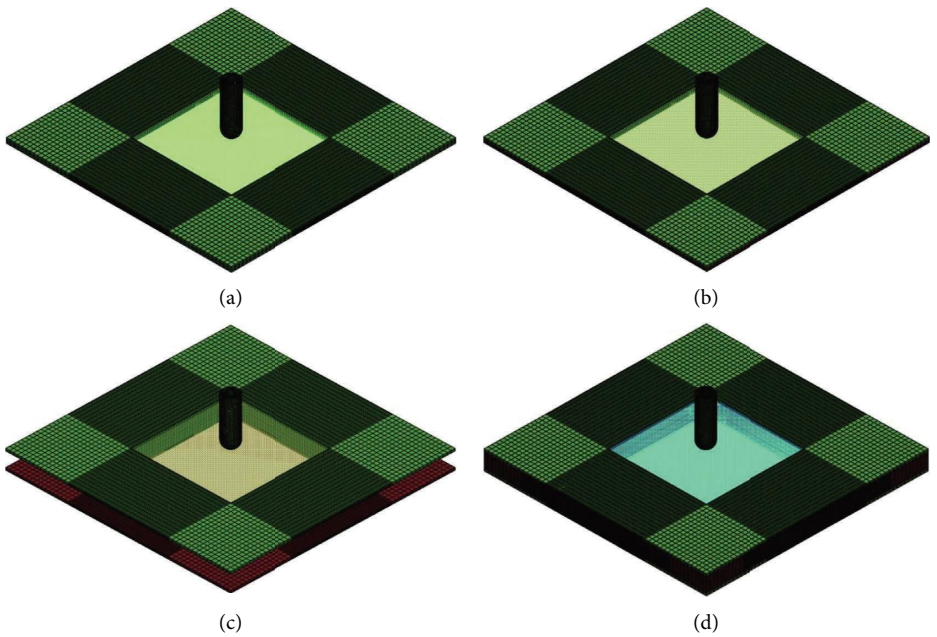

FIGURE 13: SPH-FEM model of different types of target plates and hemispherical-nosed projectile. (a) The target plate and projectile model of T8. (b) The target plate and projectile model of T4T4. (c) The target plate and projectile model of T4_12_T4. (d) The target plate and projectile model of T4_water_T4.

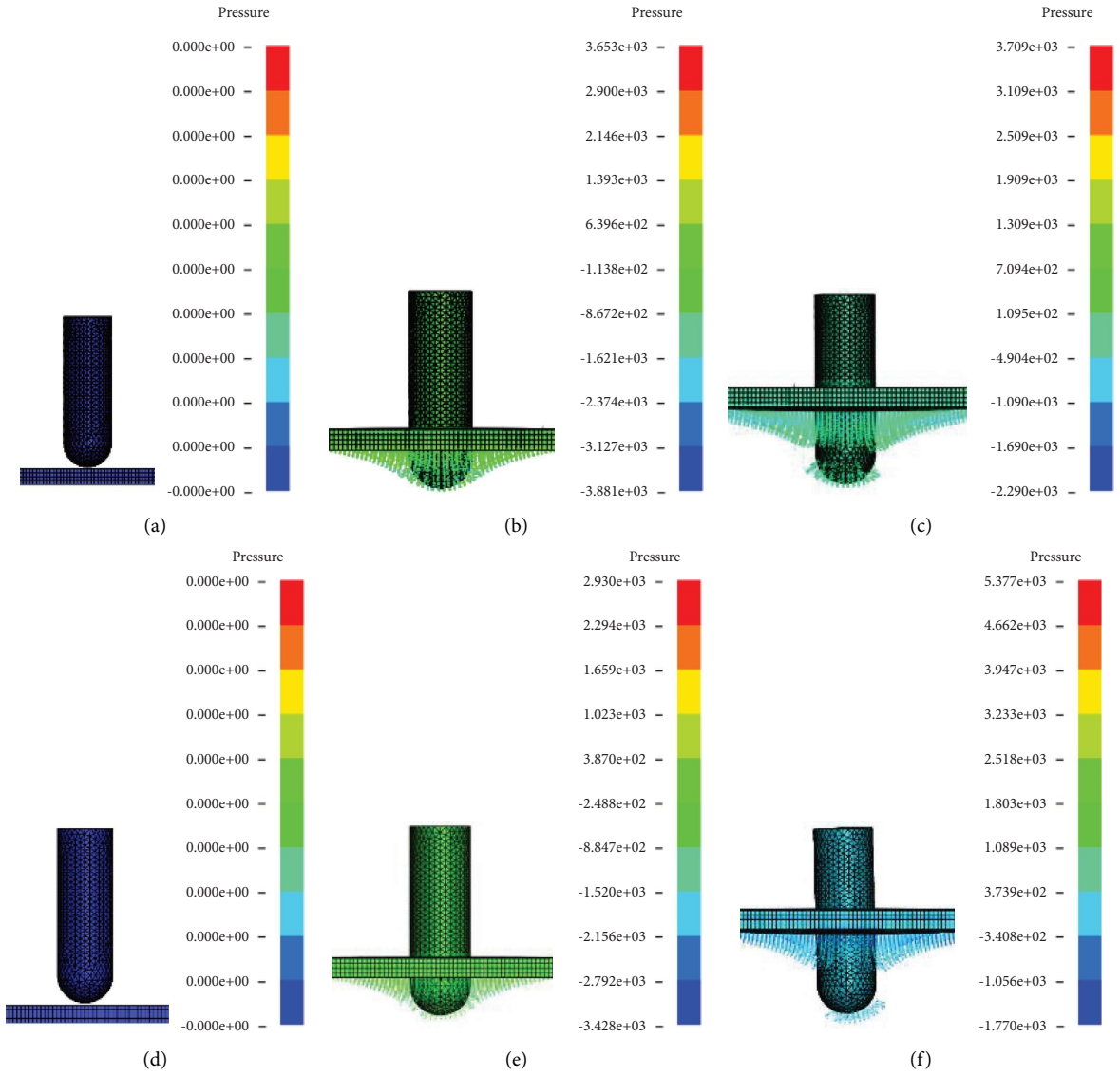

FIGURE 14: The deformation history of target plate T8 and target plate T4T4 (T8 v_i = 284.3 m/s, T4T4 v_i = 285.8 m/s). (a) *T*8 0 μs. (b) *T*8 60 μs. (c) *T*8 140 μs. (d) *T4T4* 0 μs. (e) *T4T4* 60 μs. (f) T4T4 140 μs.

T4_water_T4 with 12 mm water fluid are investigated in this section. Figure 14 illustrates the deformation process of the hemispherical-nosed projectile penetrating the single-layer target plate T8 and the in-contact double-layer target plate T4T4. The 0~140 μs deformation process of the hemispherical-nosed projectile penetration on the single-layer target plate T8 is illustrated in Figures 14(a)–14(c). When the velocity of the projectile was great enough, the target plate produced plunger, expansion, bending, and tensile deformation at the same time, and the model incurred shear and tensile damage. Figures 14(d)–14(f) shows the 0~140 μs deformation process of the in-contact double-layer target plate T4T4 penetrated by the hemispherical-nosed projectile. The target plate also appears to be punched, but compared with the single-layer target plate T8, the overall deformation and fragmentation of the in-contact double-layer target T4T4 were smaller, and as for the ballistic limit velocity, that of the in-contact double-layer target T4T4 was smaller than that of the single-layer target plate T8. We found that the coupled SPH-FEM can well handle the large deformations and ruptures of target plates.

The penetration processes of the hemispherical-nosed projectile on the double-layer target plate T4_12_T4 with 12 mm air fluid and the in-contact double-layer target plate T4T4 are shown in Figure 15. The 0~140 μs deformation process of the spaced double-layer target plate T4_12_T4 with 12 mm air fluid is shown in Figures 15(a)–15(c), and the comparison group 0~140 μs deformation process of in-contact double-layer target plate T4T4 are illustrated Figures 15(d)–15(f). It can be concluded that the T4_12_T4 target plate produced a plunger under the penetration of the hemispherical-nosed projectile, owing to the large enough spacing between the first and the second layers of target plate; the plunger of the first-layer plate influenced

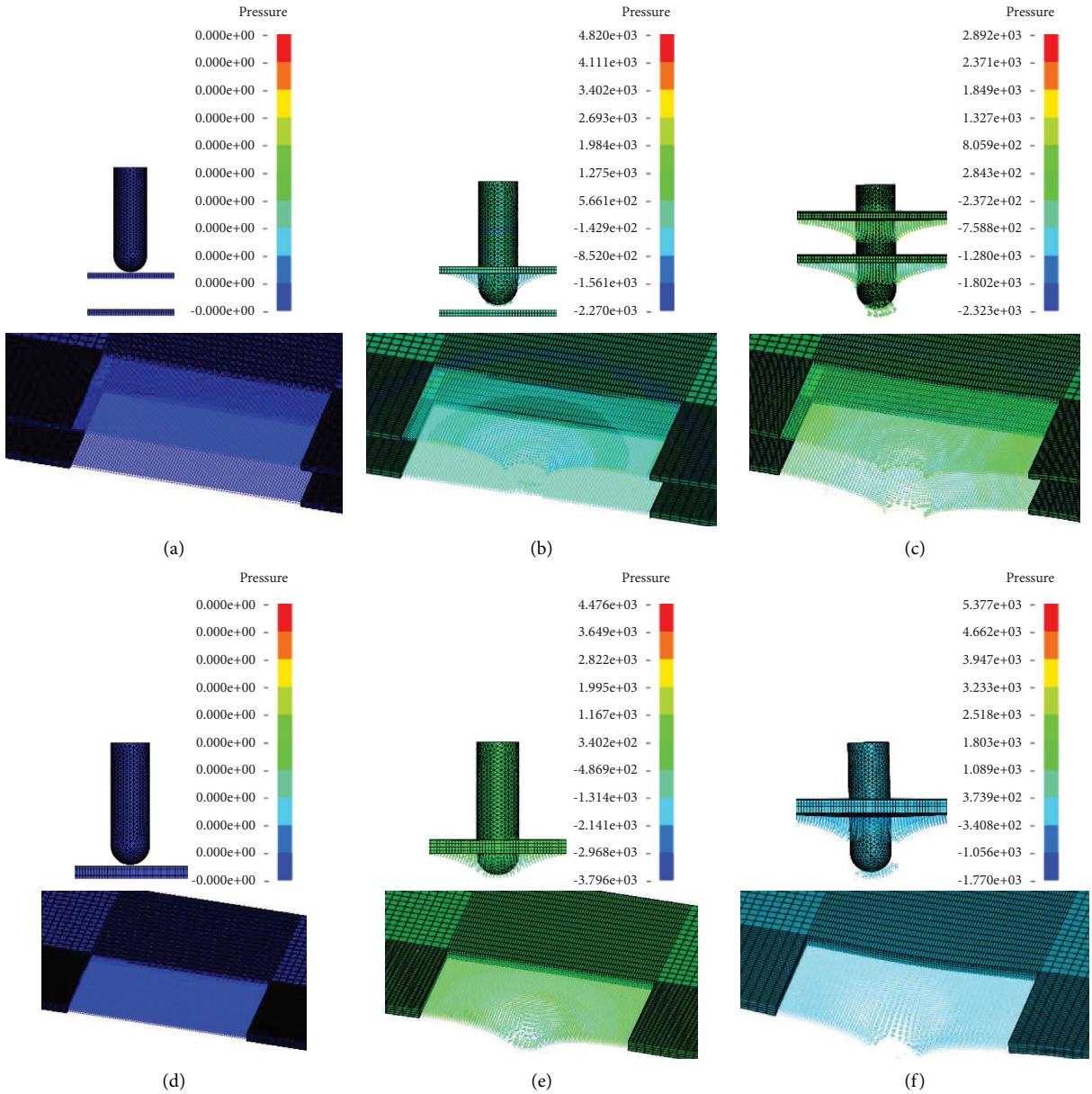

FIGURE 15: The deformation history of target plate T4_12_T4 and target plate T4T4 (T4T4 $v_i = 285.8$ m/s, T4_12_T4 $v_i = 286.7$ m/s). (a) T4_12_T4 0 μs. (b) T4_12_T4 50 μs. (c) T4_12_T4 140 μs. (d) T4T4 0 μs. (e) T4T4 50 μs. (f) T4T4 140 μs.

the second target plate with the projectile, and the second plate also produced a plunger. It can be concluded from the illustration that the plunger of the second-layer target plate was bigger than that of the first-layer target plate. Both of them produced dishing, bending, and tensile deformation. The fragment sizes of T4_12_T4 and T4T4 were determined by the particle numbers of the disconnected target plate, and it was obvious that the fragment size of T4T4 was bigger than T4_12_T4, thus proving that the antipenetration performance of the spaced double-layer target plate was better than the in-contact double-layer target plate.

The penetration processes of the hemispherical-nosed projectile on the T4_12_T4 and target plate T4_water_T4 is described in Figure 16. The 0~140 μs deformation process of target plate T4_12_T4 spaced double-layer target plate is illustrated in Figures 16(a)–16(c), and the T4_water_T4 Sandwich plate is illustrated in Figures 16(d) and 16(e). The fragment size of the target plate T4_12_T4 was bigger than the T4_water_T4 plate, but the deformation of T4_water_T4 second layer bigger than T4_water_T4, proving that the antipenetration performance of the spaced double-layer plate with the water gap better than spaced double-layer with air gap.

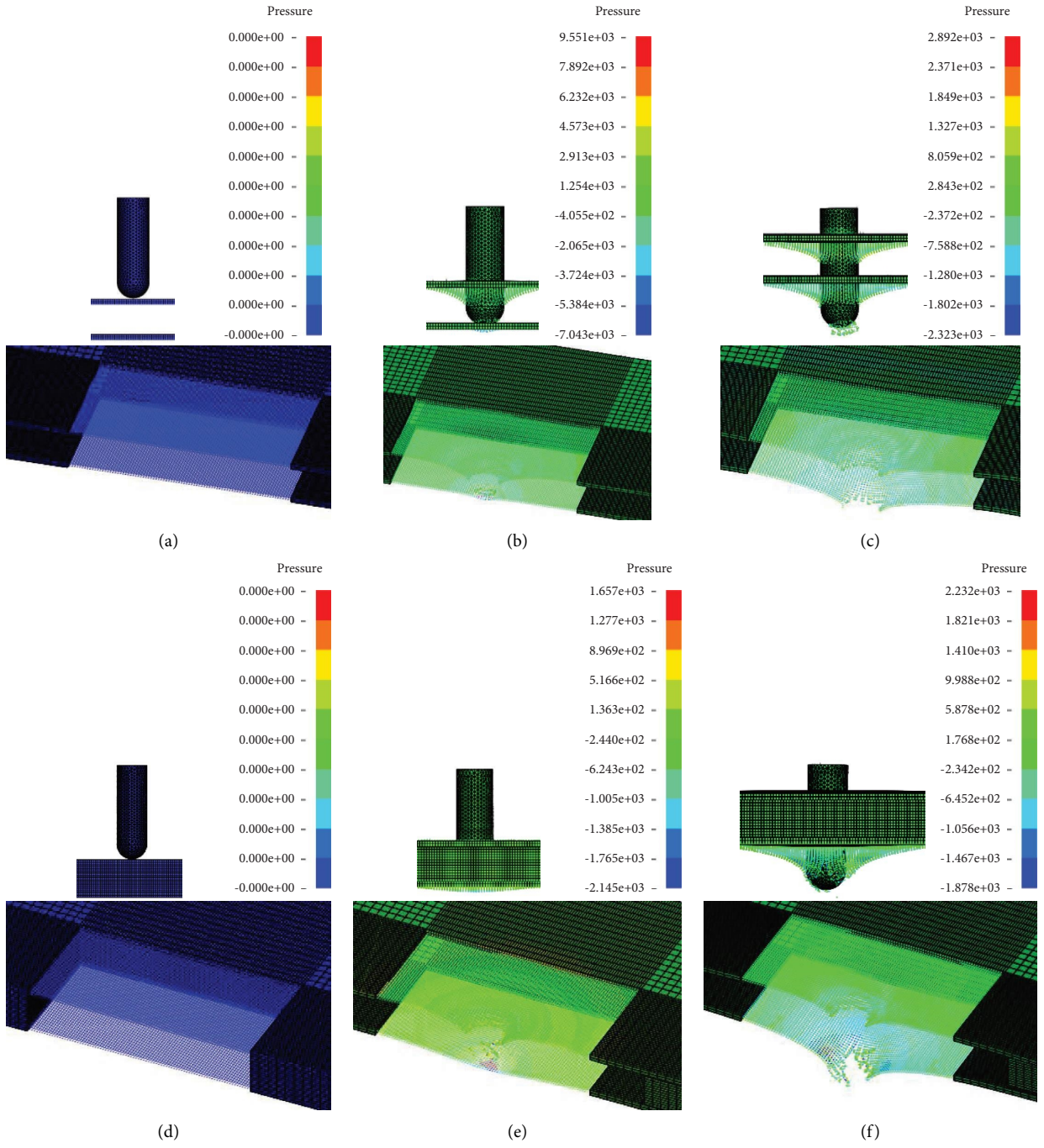

FIGURE 16: The deformation history of T4_12_T4 and T4_water_T4 target plate (T4_water_T4 $v_i = 295.6$ m/s, T4_12_T4 $v_i = 286.7$ m/s). (a) T4_12_T4 0 μs. (b) T4_12_T4 60 μs. (c) T4_12_T4 140 μs. (d) T4_water_T4 0 μs. (e) T4_water_T4 60 μs. (f) T4_water_T4 140 μs.

Figure 17 shows the change process of the water layer in the middle when the projectile penetrated the spaced double-layer plate with the water gap during over 30~150 μs. The water layer was dispersed in all directions when the projectile contacted the target plate, owing to the projectile's large diameter, and the target plate was expanded and deformed because of the interaction and extrusion between the upper and lower steel target plates. Figure 18 shows the velocity curve of the projectile, and the initial penetration velocity $v_i = 295$ m/s. The tilted part of the first section is the velocity metabolic process of the projectile striking the first layer of the steel target plate of the first layer; the slightly flat curve of the second section is the velocity changing process of the projectile striking the water layer, and the larger amplitude curve of the third section represents the velocity changing process of the projectile penetrating the second layer of the steel target plate. The reason for the large range variation in the third stage was that the velocity of the projectile decreased sharply after it impacted the first layer and the

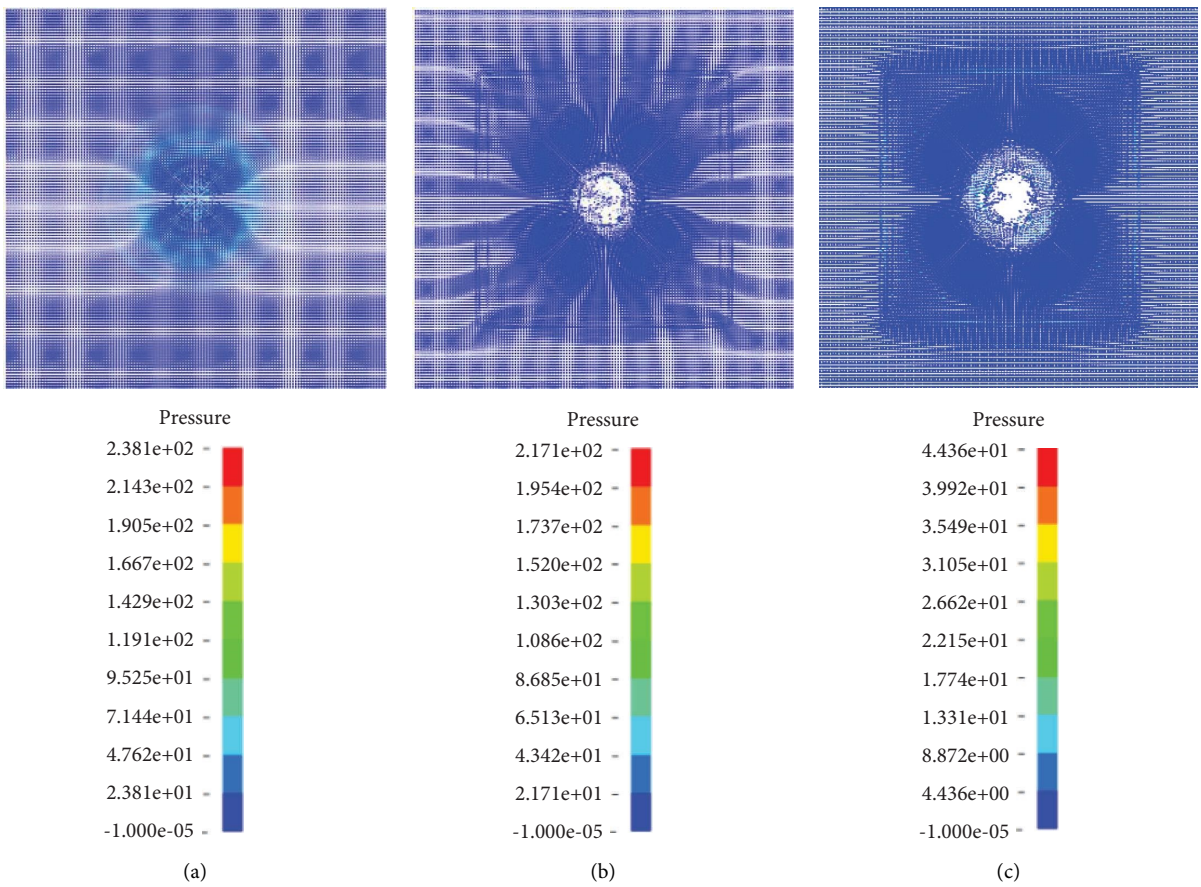

Figure 17: The deformation history of the water layer. (a) T4_water_T4 30 μs. (b) T4_water_T4 90 μs. (c) T4_water_T4 140 μs.

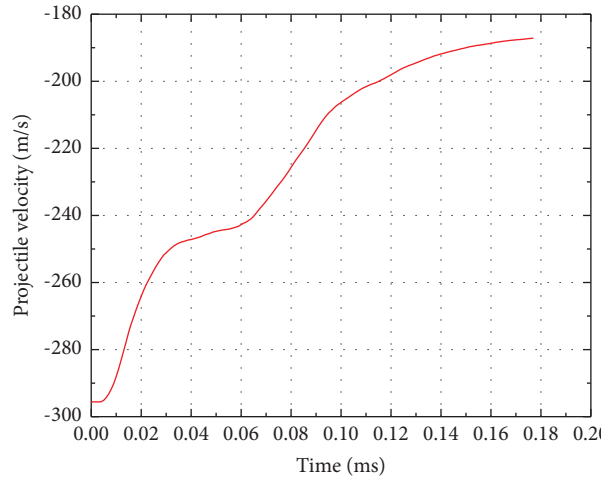

Figure 18: Velocity curve of projectile (impact velocity: 295.6 m/s).

water layer of the steel target, and it took a longer time to impact the second layer of the steel target than it did the first layer.

4.3. Penetration Velocity Analysis of Projectile. The initial-residual velocity curves of the single-layer target plate T8, in-contact double-layer target plate T4T4, spaced double-layer target plate T4_12_T4, and Sandwich plate T4_water_T4 under hemispherical-nosed projectiles are shown in Figure 19. It can be concluded from the diagram that the single-layer target plate T8 had the maximum ballistic limit velocity. The ballistic limit velocity of the spaced double-layer target T4_12_T4 with 12 mm air was the smallest, and that of the in-contact double-layer target plate T4T4 was larger than

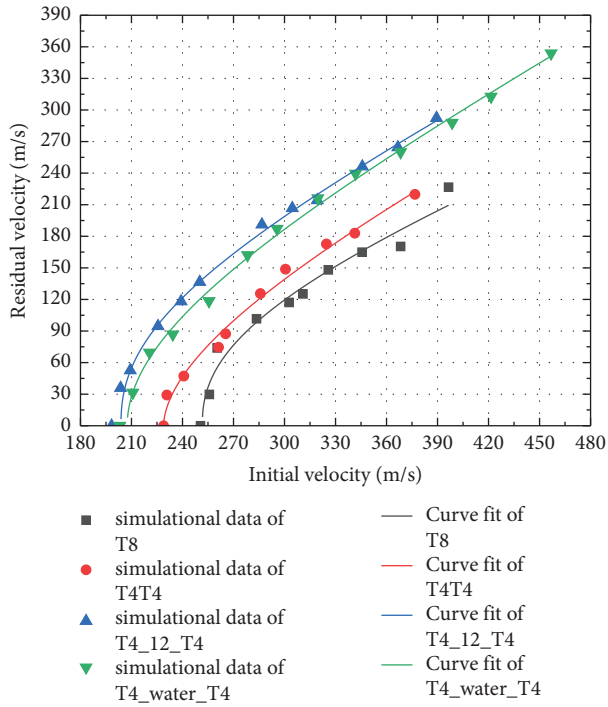

Figure 19: Residual velocity versus initial velocity under hemispherical-nosed projectiles.

that of the Sandwich plate T4_water_T4. Because the thickness of the water layer was not high enough and the size of the projectile was too large, the water layer offered little resistance to it. Through calculation, the ballistic limit velocity of the Sandwich plate T4_water_T4 was 1.035 times that of the in-contact double-layer target plate T4_12_T4 with the 12 mm air interval. The ballistic limit velocity and parameters obtained by numerical simulation corresponding to each target plate's working condition are shown in Table 8.

4.4. Deformation Analysis of One-Layer, Double-Layer, and Sandwich Target Plates. Compared with the experiment results, the influence of the number of layers of the target plate and the air space on the antipenetration performance of the target plate was determined. In this section, the coupled SPH-FEM is used to study the antipenetration performance of the single-layer target plate T8, the in-contact double-layer target plate T4T4, and the spaced double-layer target plate T4_12_T4 with the 12 mm air gap. Thus, the antipenetration of the Sandwich plate T4_water_T4 is further studied. The deformational curve of the single-layer target plate T8 and the upper target plate T4T4 in contact is shown in Figure 20. It can be seen that the deformation of the single-layer target plate T8 was greater than that of the double-layer in-contact target plate T4T4 when the initial velocity of the projectile was close. The reason is an interaction between the first and the second layers of the in-contact double-layer target plate T4T4 that offset part of the deformation, making its deformation smaller than that of the single-layer target plate. Moreover, the ballistic limit velocity of the single-layer target plate T8 was larger, and the impact time of the projectile body on the target plate was longer.

The deformations of the in-contact double-layer target plate T4T4 and the spaced double-layer target plate T4_12_T4 with a 12 mm air gap are shown in Figure 21. It can be seen that the deformation of the in-contact double-layer target plate T4T4 was larger than the spaced double-layer target plate T4_12_T4 with a 12 mm air gap. The reason is that the ballistic limit velocity of the in-contact double-layer target plate T4T4 was much larger than the double-layer target plate T4_12_T4 with the 12 mm air gap. Overall, the projectile penetrated the in-contact double-layer target plate T4T4 for a long time, resulting in a larger deformation. Moreover, the deformation of the second-layer target plate in the spaced double-layer target plate T4_12_T4 was larger than that of the first-layer target plate because the projectile penetrated the first-layer target plate and produced a plug that acted on the second-layer target plate, thus resulting in a larger deformation than the first-layer target plate. As for the deformation curve of the T4_water_T4 Sandwich target plate after impact by the projectile, we see in Figure 22 that the curve of the T4_water_T4 Sandwich target plate and the double-layer air target plate T4_12_T4 with the 12 mm air gap are shown. It can be concluded that the deformation of the steel target plate at the first layer of the Sandwich target plate T4_water_T4 was much smaller than that at the second layer. The deformation of the first and the second layers of the air double-layer target plate T4_12_T4 was larger than that of the steel target plate T4_water_T4 but smaller than that of the second layer. The reason is that the water layer in the Sandwich target plate T4_water_T4 was squeezed after being impacted by the projectile, which caused the steel

Table 8: Numerical simulation of model constants and ballistic limit velocity.

Target plate codes	a	p	v_{bl} (m/s)
T8	0.63	2.33	251.47
T4T4	0.79	1.78	228.88
T4_12_T4	0.84	2.17	200.89
T4_water_T4	0.86	1.98	207.49

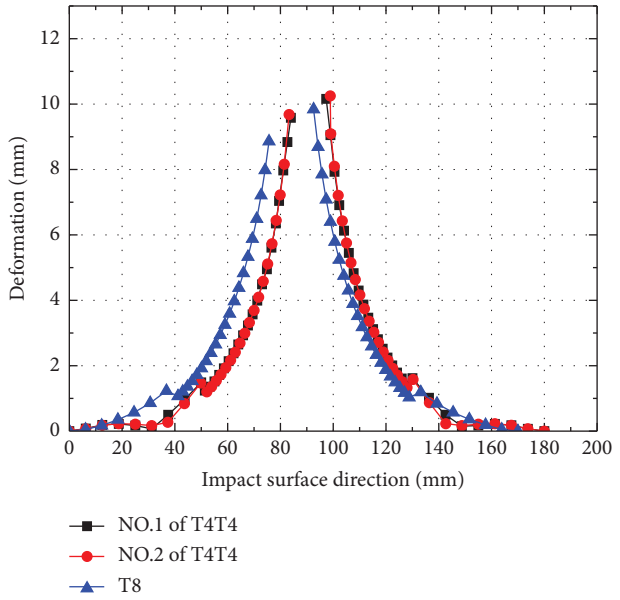

Figure 20: Deformation profiles of T4T4 and T8 target plate T4T4, $v_i = 285.79$ m/s, $v_r = 125.6$ m/s; T8 $v_i = 283.54$ m/s, $v_r = 101.62$ m/s.

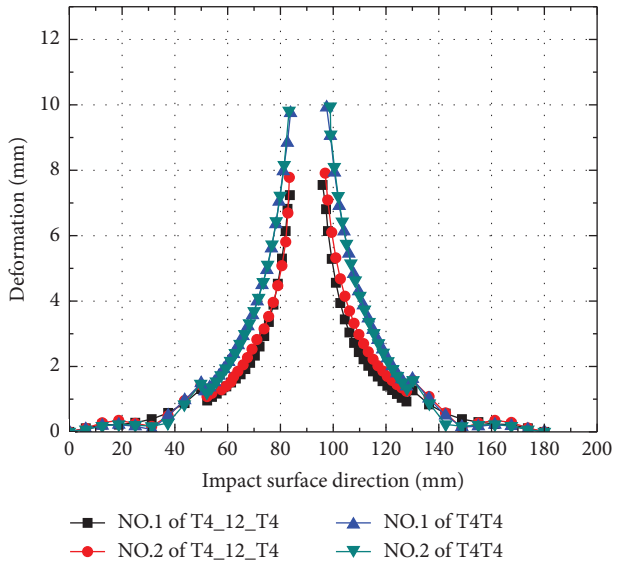

Figure 21: Deformation profiles of T4_12_T4 and T4T4 target plate. T4_12_T4, $v_i = 286.7$ m/s, $v_r = 191.15$ m/s; T4T4 $v_i = 285.79$ m/s, $v_r = 125.6$ m/s.

target plates on the upper and lower layers to expand and deform. Moreover, the action time of the target plate on the second layer was longer in the direction of projectile body penetration, resulting in larger deformation.

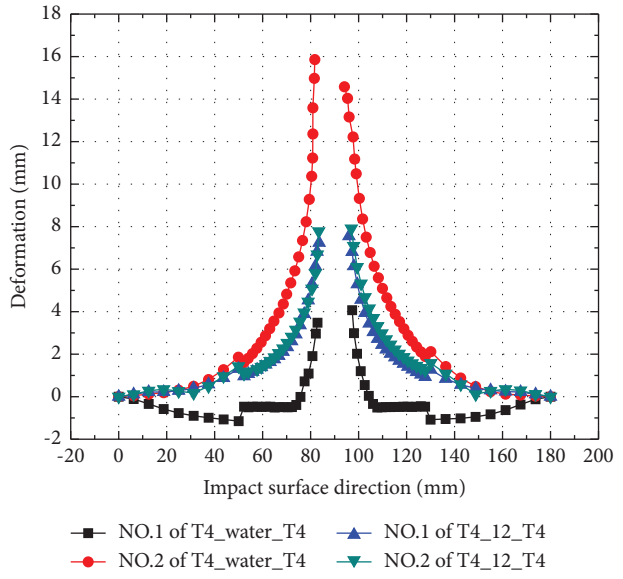

Figure 22: Deformation profiles of T4_water_T4 and T4_12_T4 T4_water_T4, $v_i = 295.59$ m/s, $v_r = 187.14$ m/s; T4_12_T4, $v_i = 286.7$ m/s, $v_r = 191.15$ m/s.

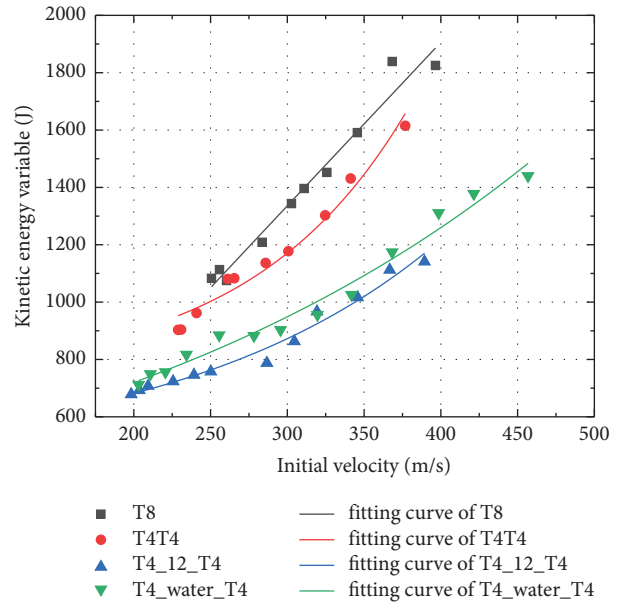

Figure 23: Kinetic energy variable vs. initial velocity for one-layer, double-layer, and sandwich target plates.

4.5. Energy Analysis of One-Layer, Double-Layer, and Sandwich Target Plates. The comparison between kinetic energy variables of T8, T4T4, T4_12_T4, and T4_water_T4 plates are shown in Figure 23, it can be seen that the result accords

with the law of kinetic energy. According to the curve changes in Figure 23 can be analyzed that the increase in the impact velocity of projectiles results in an increase in the energy dissipation. The single-layer (T8) has the best effect on energy absorption, while the energy absorption effect of T4_12_T4 is the worst when the impact velocity is the same. With the increase in initial velocity, the kinetic energy of the projectile changes more.

5. Conclusions

In this paper, the coupled SPH-FEM was used to study the antipenetration performance of single- and multilayer plates subjected to high-speed hemispherical-nosed projectiles. The feasibility and accuracy were validated by comparing them with the experimental results, and on this basis, the single-layer and multilayer Sandwich target plates are studied. The main conclusions of this study were as follows:

(1) The initial-residual velocity of the hemispherical-nosed projectile, the deformational process and damage to single- and multilayer target plates based on the coupled SPH-FEM were compared with the experimental results. The comparison indicated that the coupled SPH-FEM had high reliability and accuracy, and was suitable for the antipenetration analysis of high-velocity, large deformation, and multilayer hetero structures.

(2) The gap medium greatly influences the ballistic limit velocity of double-layer target plates. The single-layer (T8) had the highest ballistic limit velocity, followed by the in-contact double-layer target plate (T4T4), the water gap double-layer target plate (T4_water_T4), and the air gap double-layer (T4_12_T4) had the lowest ballistic limit velocity.

(3) Water had the greatest influence on the deformation of the double-layer target plate, the difference between T4_water_T4 top and bottom plate deformations was the biggest. The deformation of the T4T4 and T4_12_T4 top and bottom plates was basically equal.

(4) The single-layer (T8) has the best ability for energy absorption, while the energy absorption effect of T4_12_T4 is the worst. With the increase in initial velocity, the kinetic energy of the projectile changes more.

Data Availability

The data used to support the findings of this study are included within the article.

Conflicts of Interest

The authors declare that they have no conflicts of interest.

Acknowledgments

This study was supported financially by the National Natural Science Foundation of China (Grant no. 52001145) and the Natural Science Foundation of Jiangsu Province of China (BK20180976).

References

[1] A. Bhat, J. Naveen, M. Jawaid, M. N. F. Norrrahim, A. Rashedi, and A. Khan, "Advancement in fiber reinforced polymer, metal alloys and multi-layered armour systems for ballistic applications – a review," *Journal of Materials Research and Technology*, vol. 15, pp. 1300–1317, 2021.

[2] G. Ben-Dor, A. Dubinsky, and T. Elperin, "New results on ballistic performance of multi-layered metal shields: review," *Theoretical and Applied Fracture Mechanics*, vol. 88, pp. 1–8, 2017.

[3] Z. Wei, D. Yunfei, C. Z. Sheng, and W. Gang, "Experimental investigation on the ballistic performance of monolithic and layered metal plates subjected to impact by blunt rigid projectiles," *International Journal of Impact Engineering*, vol. 49, pp. 115–129, 2012.

[4] Y. Deng, W. Zhang, and Z. Cao, "Experimental investigation on the ballistic resistance of monolithic and multi-layered plates against ogival-nosed rigid projectiles impact," *Materials and Design*, vol. 44, pp. 228–239, 2013.

[5] Y. Deng, W. Zhang, and Z. Cao, "Experimental investigation on the ballistic resistance of monolithic and multi-layered plates against hemispherical-nosed projectiles impact," *Materials and Design*, vol. 41, pp. 266–281, 2012.

[6] N. Zhao, R. Ye, A. Tian, J. Cui, P. Ren, and M. Wang, "Experimental and numerical investigation on the antipenetration performance of metallic sandwich plates for marine applications," *Journal of Sandwich Structures & Materials*, vol. 22, no. 2, pp. 494–522, 2020.

[7] T. Ali, Y. Peng, Z. Jinhao, L. Kun, and Y. Renchuan, "Crashworthiness optimization method for sandwich plate structure under impact loading," *Ocean Engineering*, vol. 250, Article ID 110870, 2022.

[8] E. Ahmadi, A. Atrian, J. J. Fesharaki, H. Montazerolghaem, and S. Saberi, "Experimental and numerical assessment of high-velocity impact behavior of syntactic foam core sandwich structures," *European Journal of Mechanics-A: Solids*, vol. 90, Article ID 104355, 2021.

[9] M. Abbasi and A. Alavi Nia, "High-velocity impact behavior of sandwich structures with AL faces and foam cores—experimental and numerical study," *Aerospace Science and Technology*, vol. 105, Article ID 106039, 2020.

[10] P. Ren, Q. Tao, L. Yin et al., "High-velocity impact response of metallic sandwich structures with PVC foam core," *International Journal of Impact Engineering*, vol. 144, Article ID 103657, 2020.

[11] R. Ye, N. Zhao, D. Yang, J. Cui, O. Gaidai, and P. Ren, "Bending and free vibration analysis of sandwich plates with functionally graded soft core, using the new refined higher-order analysis model," *Journal of Sandwich Structures & Materials*, vol. 23, no. 2, pp. 680–710, 2020.

[12] X. Zhang, R. Wang, J. Liu, X. Li, and G. Jia, "A numerical method for the ballistic performance prediction of the sandwiched open cell aluminum foam under hypervelocity impact," *Aerospace Science and Technology*, vol. 75, pp. 254–260, 2018.

[13] M. H. Siemann and S. A. Ritt, "Novel particle distributions for SPH bird-strike simulations," *Computer Methods in Applied Mechanics and Engineering*, vol. 343, pp. 746–766, 2019.

[14] A. Riccio, R. Cristiano, S. Saputo, and A. Sellitto, "Numerical methodologies for simulating bird-strike on composite wings," *Composite Structures*, vol. 202, pp. 590–602, 2018.

[15] J. Kwon and J. J. Monaghan, "A novel SPH method for sedimentation in a turbulent fluid," *Journal of Computational Physics*, vol. 300, pp. 520–532, 2015.

[16] L. Deng, Y. Liu, W. Wang, W. Ge, and J. Li, "A two-fluid smoothed particle hydrodynamics (TF-SPH) method for gas–solid fluidization," *Chemical Engineering Science*, vol. 99, pp. 89–101, 2013.

[17] A. Khayyer, Y. Shimizu, H. Gotoh, and S. Hattori, "A 3D SPH-based entirely Lagrangian meshfree hydroelastic FSI solver for anisotropic composite structures," *Applied Mathematical Modelling*, vol. 112, pp. 560–613, 2022.

[18] D. Feng and R. Imin, "A kernel derivative free SPH method," *Results in Applied Mathematics*, vol. 17, Article ID 100355, 2023.

[19] Y. Zhao, Z. Zhou, J. Bi, C. Wang, and Z. Wu, "Numerical simulation the fracture of rock in the framework of plastic-bond-based SPH and its applications," *Computers and Geotechnics*, vol. 157, Article ID 105359, 2023.

[20] B. Xue, Y. X. Peng, S.-F. Ren, N.-N. Liu, and Q. Zhang, "Investigation of impact resistance performance of pyramid lattice sandwich structure based on SPH-FEM," *Composite Structures*, vol. 261, Article ID 113561, 2021.

[21] Z. Wu, F. Yu, P. Zhang, and X. Liu, "Micro-mechanism study on rock breaking behavior under water jet impact using coupled SPH-FEM/DEM method with Voronoi grains," *Engineering Analysis with Boundary Elements*, vol. 108, pp. 472–483, 2019.

[22] H. Zhong, L. Lyu, Z. Yu, and C. Liu, "Study on mechanical behavior of rockfall impacts on a shed slab based on experiment and SPH–FEM coupled method," *Structures*, vol. 33, pp. 1283–1298, 2021.

[23] Y. Zhou, Y. Sun, T. Huang, and W. Cai, "SPH-FEM simulation of impacted composite laminates with different layups," *Aerospace Science and Technology*, vol. 95, Article ID 105469, 2019.

[24] Z. Zhang, L. Wang, V. V. Silberschmidt, and S. Wang, "SPH-FEM simulation of shaped-charge jet penetration into double hull: a comparison study for steel and SPS," *Composite Structures*, vol. 155, pp. 135–144, 2016.

[25] Y. Wang, Y. He, T. Zhang, X. Fan, and T. Zhang, "Damage analysis of typical structures of aircraft under high-velocity fragments impact," *Alexandria Engineering Journal*, vol. 62, pp. 431–443, 2023.

[26] R. Scazzosi, M. Giglio, and A. Manes, "FE coupled to SPH numerical model for the simulation of high-velocity impact on ceramic based ballistic shields," *Ceramics International*, vol. 46, no. 15, pp. 23760–23772, 2020.

[27] D. Yongjun, W. Yi, Q. Kefo, and Y. Yong, "Ballistic performance of multi-layered B4C ceramic and UHMWPE fibre laminate targets subjected to hypervelocity impact by tungsten alloy ball," *Structures*, vol. 45, pp. 542–559, 2022.

[28] Z.-T. Cheng, Z. Xiang, and Q. Song, "FEM-SPH adaptive method for analysis protection mechanism of B4C ceramics," *Engineering Failure Analysis*, vol. 148, Article ID 107207, 2023.

[29] M. R. I. Islam and A. Shaw, "Pseudo-spring SPH simulations on the perforation of metal targets with different damage models," *Engineering Analysis with Boundary Elements*, vol. 111, pp. 55–77, 2020.

[30] Q. Tao, P. Ren, L. Shi et al., "Energy absorption and impact behavior of composite sandwich panels under high-velocity spherical projectile," *International Journal of Impact Engineering*, vol. 162, Article ID 104143, 2022.

[31] P. Ren, J. Zhou, A. Tian, R. Ye, L. Shi, and W. Zhang, "Experimental investigation on dynamic failure of water-filled vessel subjected to projectile impact," *International Journal of Impact Engineering*, vol. 117, pp. 153–163, 2018.

[32] J. J. Monaghan, "Smoothed particle hydrodynamics," *Annual Review of Astronomy and Astrophysics*, vol. 30, no. 1, pp. 543–574, 1992.

[33] J. J. Monaghan, "Smoothed particle hydrodynamics," *Reports on Progress in Physics*, vol. 68, no. 8, pp. 1703–1759, 2005.

[34] W. Wang, Y. Wu, H. Wu, C. Yang, and Q. Feng, "Numerical analysis of dynamic compaction using FEM-SPH coupling method," *Soil Dynamics and Earthquake Engineering*, vol. 140, Article ID 106420, 2021.

[35] J. O. Hallquist, *LS-DYNA Theory Manual*, Livermore software Technology Corporation, Livermore, CA, USA, 2006.

[36] F. H. Lee and Q. Gu, "Method for estimating dynamic compaction effect on sand," *Journal of Geotechnical and Geoenvironmental Engineering*, vol. 130, no. 2, pp. 139–152, 2004.

[37] J. Halquist, *LS-DYNA Keyword User's Manual Version 971*, Livermore Software Technology Corporation, Livermore, CA, USA, 2007.

[38] T. Børvik, O. S. Hopperstad, T. Berstad, and M. Langseth, "A computational model of viscoplasticity and ductile damage for impact and penetration," *European Journal of Mechanics-A: Solids*, vol. 20, no. 5, pp. 685–712, 2001.

[39] G. R. Johnson, "A constitutive model and data for materials subjected to large strains, high strain rates, and high temperatures," in *Proceedings of the 7th International Symposium on Ballistics*, pp. 541–547, The Hague, The Netherlands, September 1983.

[40] T. Børvik, S. Dey, and A. H. Clausen, "Perforation resistance of five different high-strength steel plates subjected to small-arms projectiles," *International Journal of Impact Engineering*, vol. 36, no. 7, pp. 948–964, 2009.

[41] E. A. Flores-Johnson, M. Saleh, and L. Edwards, "Ballistic performance of multi-layered metallic plates impacted by a 7.62-mm APM2 projectile," *International Journal of Impact Engineering*, vol. 38, no. 12, pp. 1022–1032, 2011.

[42] X. Xiao, *The Ballistic Resistance of Double-Layered Metallic Target and the Deformation and Fracture of Taylor Rod*, Harbin Institute of Technology, Harbin, China, 2010.

[43] S. Dey, T. Børvik, X. Teng, T. Wierzbicki, and O. S. Hopperstad, "On the ballistic resistance of double-layered steel plates: an experimental and numerical investigation," *International Journal of Solids and Structures*, vol. 44, no. 20, pp. 6701–6723, 2007.

[44] L. Olovsson, S. Mhamed, and I. Do, *LS DYNA ALE Capabilities (Arbitrary-Lagrangian-Eulerian) Fluid-Structure Interaction Modeling*, Livermore software Technology Corporation, Livermore, CA, USA, 2003.

[45] Q. X. Xu, *Research on Some Problems of Impact Dynamics Based on SPH Method*, Shanghai Jiao Tong University, Shanghai, China, 2009.

[46] R. F. Recht and T. W. Ipson, "Ballistic perforation dynamics," *Journal of Applied Mechanics*, vol. 30, no. 3, pp. 384–390, 1963.